PHYSICAL REVIEW B **109**, 024101 (2024)

Editors' Suggestion

Experimental and computational study of the core-level crossing transition in iridium at high pressure

C. V. Storm,[*] G. A. Woolman, C. M. Lonsdale, J. D. McHardy, M. J. Duff, G. J. Ackland, and M. I. McMahon
SUPA, School of Physics & Astronomy, and Center for Science at Extreme Conditions, The University of Edinburgh,
Peter Guthrie Tait Road, Edinburgh EH9 3FD, United Kingdom

(Received 26 September 2023; accepted 27 November 2023; published 3 January 2024)

A core-level crossing (CLC) resulting from extreme compression has been calculated to occur in Ir metal at 80 GPa, analogous to a transition previously reported in Os at 392 GPa. We present results from static high-pressure diffraction experiments and theoretical investigations on the compressive behavior of Ir up to 159 GPa, well above the calculated CLC transition pressure. Neither our experimental nor computational results find evidence for a CLC over this pressure range, and instead, our first-principles calculations suggest that the CLC occurs in Ir at the much higher pressure of 400 GPa. Furthermore, computational analysis of the CLC in Ir, combined with previous work on Os, indicates that CLCs at high pressure are not experimentally detectable.

DOI: 10.1103/PhysRevB.109.024101

I. INTRODUCTION

On compression, the relative motion of different electron levels can result in various effects in materials at high pressures, such as electron transfer in the alkali metals [1,2] and lanthanides [3], metallization [4,5], and changes in the topology of the Fermi surface (a so-called electronic topological transition, or ETT) [6].

Such effects all arise from changes in the interactions between the atoms' outer valence electrons and have readily observable consequences in bulk material properties, such as compressibility or unit-cell axial ratios. However, compression can affect the inner core electrons too, and core electron levels can be measured using Auger spectroscopy and calculated by electronic structure methods [7]. The core-level energies are known to be pressure dependent, and in some materials pressure can lead to a so-called core-level crossing (CLC) transition.

In Os, an anomaly in the hexagonal c/a ratio was reported to arise as a result of a CLC, where broadening of the low-lying $5p$ states causes $5p_{3/2}$ and $4f_{7/2}$ states to start interacting with each other at 392 GPa [8]. Inspired by this experimental result, Tal *et al.* performed a series of electronic structure calculations of CLCs in the $5d$ metals Hf, Ta, W, Re, Os, Ir, Pt, and Au [9]. They found the CLC transition to be a general effect in all of these metals, with the transition pressure varying from ~1500 GPa in Pt down to only 80 GPa in Ir, and even ambient pressure in Ref. [9]. However, a recent paper by Woolman and Ackland [10] cast doubt on the suggestion by Dubrovinsky *et al.* [8] that core-level crossings perturb the crystal structure. This then calls into question if CLCs have any detectable effect on the crystal structure [10]. The current work examines Ir to see if any connection between the proposed CLC and crystal structure can be detected.

Ir is cubic, so, unlike hexagonal Os, changes in the c/a axial ratio cannot be used to identify the CLC transition. However, Tal *et al.* hypothesized that the CLC transition might lead to a change in, or anomaly in, the compressibility [9], a possibility discussed previously for Os [8]. Density functional theory (DFT) is the perfect method for testing this hypothesis, as it is capable of both locating the CLC and determining the compressibility in the same calculation, and since we are looking for a correlation rather than a precise pressure, all numerical and methodological errors will cancel out.

There have been six previous diffraction studies of the compressibility of Ir [11–16], although only the study by Monteseguro *et al.* [15] measured the compressibility to above the calculated pressure of the CLC transition. However, even below 80 GPa, the compressibility data from these studies show a surprisingly large degree of variation (see Sec. II). Such disagreements may have arisen both from difficulties in compressing a hard metal such as Ir without incurring the effects of deviatoric stress, and Ir's very high bulk modulus that requires very-high-quality compression data.

We have recently shown that Bi is an excellent pressure-transmitting medium (PTM) up to 300 GPa and that it can also be used as a pressure calibrant [17]. We have therefore studied the compressibility of Ir in a Bi PTM to a maximum pressure of 159 GPa, well above the calculated CLC transition pressure. We see no clear evidence of an anomaly in the compression curve or the bulk modulus which would indicate a CLC transition.

The rest of this paper is organized as follows. After a review of the previous compressibility studies of Ir in Sec. II, we describe our own experimental and data analysis techniques in Sec. III. In particular, we perform a linearization

---

[*] cstorm@ed.ac.uk

TABLE I. A summary of previous compressibility studies of Ir, giving the ambient pressure volume, the bulk modulus (K_0) and its pressure derivative (K_0'), the PTM used (M:E=4:1 methanol:ethanol), and the maximum pressure reached. All values were obtained by fitting experimental data with the same Birch-Murnaghan EoS. For the value of V_0 in Yusenko *et al.* [14], we have used their published volume of 56.56(24)Å^3, but note that this is inconsistent with their published ambient pressure lattice parameter.

Author	V_0 (Å^3/cell)	K_0 (GPa)	K_0'	PTM	P_{max} (GPa)
Akella [11]				M:E	30
Cerenius and Dubrovinsky [12]	56.69(7)	306(23)	6.8(15)	MgO	65
Cynn *et al.* [13]	56.58(11)	383(14)	3.1(8)	Ar	55
Yusenko *et al.* [14]	56.56(24)	341(10)	4.7(3)	Ne	67.5
Monteseguro *et al.* [15]	56.48	339(3)	5.3(1)	He	137
Anzellini *et al.* [16]	56.48(9)	360(5)	6.0(5)	MgO	35

of the compressibility data using Holzapfel's equation of state (EoS) formalism, which we have recently demonstrated can reveal subtle changes in compressibility that arise from electron-transfer effects in the lanthanide [18–21] and alkali metals [22]. After showing our experimental results in Sec. IV, we describe DFT electronic structure calculations on the same system in Sec. V.

II. PREVIOUS DIFFRACTION STUDIES OF THE COMPRESSIBILITY OF IRIDIUM

The results from the six previous studies of the compressibility of Ir using x-ray diffraction are summarized in Table I [11–16]. Given that the great majority of the other elements in the periodic table have been studied to pressures in excess of 100 GPa, the paucity of very-high-pressure data on Ir is striking, and perhaps an indication of the experimental difficulties in studying such a hard, incompressible material, despite it being a strong scatterer of x rays. Fortuitously, the one previous study of Ir to above 100 GPa, by Monteseguro *et al.* [15], used a He PTM in their study, which is generally regarded as being the best PTM for high-pressure studies.

Also noteworthy is the variation in the parameters obtained in the previous studies by fitting the same Birch–Murnaghan EoS to the compression curves, with K_0 varying by 25%, and K_0' by a factor of more than 2 (see Table I). The differences are likely to have arisen from variations in the sample environments, as well as the difficulties in fitting EoSs to data collected over a limited pressure range from a highly incompressible sample.

While the authors of each of these studies showed typical *P*-*V* compression curves, which are all plotted in Fig. 1(a), the subtle changes in compression that might arise from the CLC transition are unlikely to be visible in such plots. However, we have recently demonstrated that compressibility changes are more readily observed in linearized compressibility plots [22], particularly using Holzapfel's adapted polynomial of order L (APL) EoS formalism [23,24].

Linearization and analysis of previous data

We examine previous compression data in the context of the APL EoS formalism:

$$P(x) = 3K_0 \frac{(1-x)}{x^5} e^{c_0(1-x)} \left[1 + x \sum_{k=2}^{L} c_k (1-x)^{k-1} \right], \quad (1)$$

where K_0 is the zero-pressure bulk modulus, K_0' is its pressure derivative, $x = (V/V_0)^{1/3}$, $c_0 = -\ln(3K_0/P_{\mathrm{FG0}})$, $c_2 = (3/2)(K_0' - 3) - c_0$, c_k are independent fitting parameters for

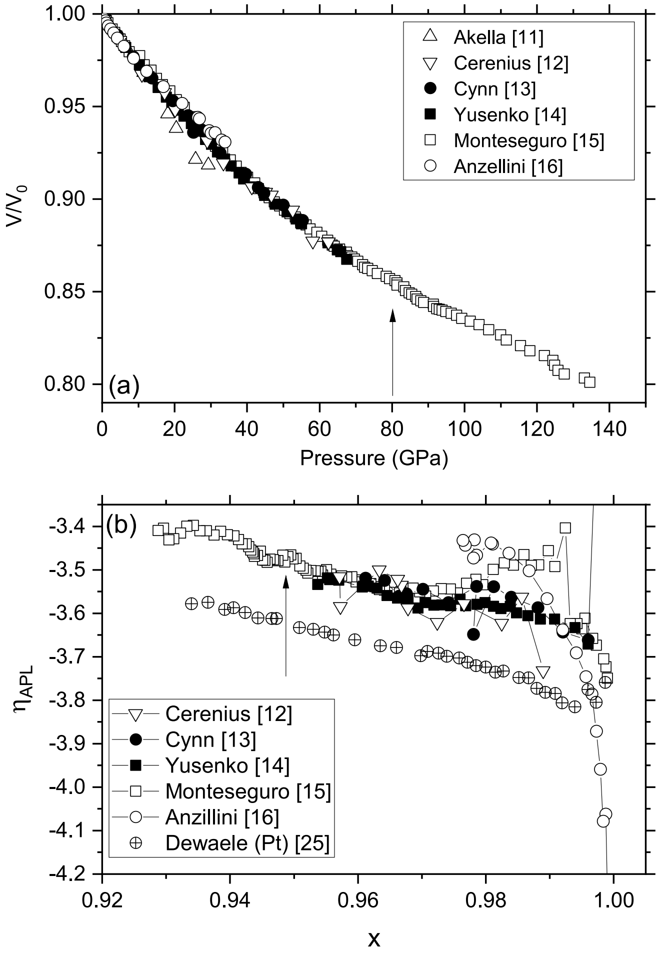

FIG. 1. The compressibility (a) and linearized compressibility (b) of Ir, as published in previous diffraction studies. In linearizing the data, we used the published V_0 from each study. The data from Akella are not shown in linearized form as no value of V_0 was provided in that study. The lowest-pressure data points from Yusenko and Anzellini lie off the top and bottom of the graph, respectively. Also shown for comparison are the linearized data for Pt, the neighboring element to Ir, using the data from Dewaele *et al.* [25]. The arrows in each plot identify the location of the proposed CLC at 80 GPa.

$k \in [3..L]$, $P_{\mathrm{FG0}} = a_{\mathrm{FG0}}(Z/V_0)^{(5/3)}$ is the Fermi-gas pressure, Z is the atomic number, and $a_{\mathrm{FG0}} = 2337$ GPa Å^5 is a constant. Note that in the lowest-order AP1 ($L = 1$) case, the summation term is zero and the only refinable parameters are the ambient volume (V_0) and bulk modulus (K_0), with K_0' being calculated from $K_0' = 3 + (2/3)c_0$.

In discussing the compressive behavior of elements with very high bulk moduli, such as Ir, it is instructive to linearize the compression data to accentuate changes in compressive behavior in a so-called $\eta_{\mathrm{APL}} - x$ plot. In the APL formalism with $L = 1$, this linearization results in

$$\eta_{\mathrm{APL}}(x) = \ln\left(\frac{Px^5}{P_{\mathrm{FG0}}(1-x)}\right), \qquad (2)$$

with variables and constants as in Eq. (1). Thus in the APL formalism an "ideal" or "simple" metal is well described by a first-order AP1 EoS and exhibits linear behavior with

$$\lim_{x\to 1} \eta_{\mathrm{APL}}(x) = \ln\left(\frac{3K_0}{P_{\mathrm{FG0}}}\right)$$

and

$$\lim_{x\to 0} \eta_{\mathrm{APL}}(x) = 0.$$

The linearized compression data from five of the previous six studies of Ir are shown in Fig. 1(b) (the sixth, earliest study by Akella [11] did not report a value of V_0, which is needed for the linearization) in the form of a $\eta_{\mathrm{APL}} - x$ plot. Also shown for comparison is the linearized compressibility of Ir's neighboring element Pt, as determined by Dewaele *et al.* [25].

It is immediately clear that there is a great deal of scatter between the different sets of linearized data for Ir, and, with the possible exception of the data by Yusenko *et al.* [14], the individual data sets do not have the simple linear trend exhibited by Pt. At large values of x (low pressures), the linearized data of both Monteseguro *et al.* [15] and Anzellini *et al.* [16] show significant discontinuities and strongly nonlinear behavior. This can arise from an incorrect value of V_0, and it is clear from Table I that the same value of V_0 in both these studies is markedly lower than those reported in the other three studies.

The arrows in Fig. 1 identify the location of the CLC proposed by Tal *et al.* [9] at 80 GPa. While the linearized data of Monteseguro *et al.* shows a small dip at pressures slightly above 80 GPa, the change is transient and is much smaller than the discontinuity seen, for example, in the same study at $x \sim 0.992$ (8 GPa). While the linearized data of Yusenko *et al.* show a trend most similar to Pt, the highest pressure reached in that study was only 67.5 GPa. In summary, there are no features in the linearized data from any previous study indicative of a change in compressibility associated with a CLC.

The scatter seen in Fig. 1(b) is likely to have arisen because of Ir's extremely low compressibility and high hardness. Even in studies conducted using a soft PTM, such as Ne [14], Ar [13], or He [15], their very high compressibility at low pressures, particularly if loaded as a high-pressure gas, can lead to the collapse of the gasket hole. This risks the Ir sample bridging between the two diamond anvils, resulting in strongly nonhydrostatic stresses.

III. EXPERIMENTAL METHOD

We have recently shown that Bi is an excellent PTM to multimegabar pressures and that at 298 GPa it supports a uniaxial stress component t of less than 0.5 GPa [17], comparable to He at the same pressures. Also, as the Bi is loaded as a solid, it is easy to ensure that the sample is completely encased in the PTM prior to compression, improving the hydrostaticity of the pressure environment and helping to prevent bridging.

Polycrystalline Ir was compressed in diamond anvil cells (DACs) equipped with anvils with 300-μm culets bevelled to 100 μm. In each DAC, a small grain of Ir powder with a diameter of ∼5 μm was placed between two disks of Bi made by gently compressing small, as-bought Bi spheres. The sample chamber had an initial diameter of 50 μm and was lined with Bi so that the Ir sample was completely encased before closing the cell. The Bi served as both the PTM and the pressure calibrant, using the EoS established in Storm *et al.* [17].

The diffraction data were collected on beamline P02.2 at the PETRA-III synchrotron with an x-ray wavelength of 0.4839 Å and a beam size (FWHM) of 0.85 μm × 0.85 μm [26,27]. The sample pressure was increased manually and allowed to stabilize for at least 5 min before the x-ray exposures were taken. The typical exposure time was 10 s, and the diffraction data were collected at pressure increments of ∼5 GPa. The highest pressure reached was 159 GPa, above which the anvils failed. The 2D diffraction image and integrated profile from Ir at this pressure are shown in Fig. 2, illustrating the high data quality.

The diffraction data were recorded on a Perkin-Elmer area detector placed ∼345 mm from the sample. The exact sample-detector distance and the detector tilts were determined using a diffraction standard ($\mathrm{CeO_2}$). The two-dimensional (2D) diffraction images obtained at each pressure were integrated into standard one-dimensional (1D) profiles using DIOPTAS [28], which were then analyzed by fitting to the measured d spacings of all nonoverlapped diffraction peaks from Ir and Bi as obtained at each pressure by Gaussian peak fitting [29].

As knowledge of the pressure gradients in the sample and the hydrostaticity of the pressure environment were essential considerations in this study, we made a number of 2D grid scans across the gasket hole at approximately 10-GPa increments on compression. The 2D scans used a 19 × 19 grid with a spacing of 2 μm and a collection time of 2 s at each point.

As a number of different values of V_0 have been reported for Ir (see Table I), we determined our own value by collecting diffraction data from a grain of Ir contained within an otherwise-empty gasket hole of a centered DAC. By fitting to the measured positions of 19 Bragg peaks, we determined the ambient unit-cell volume to be 56.614(13) Å^3, and we fixed V_0 at this value in all subsequent analysis.

IV. EXPERIMENTAL RESULTS

Before presenting the results of the compressibility of Ir, we describe our measurements of the stress environment of the sample in the Bi PTM.

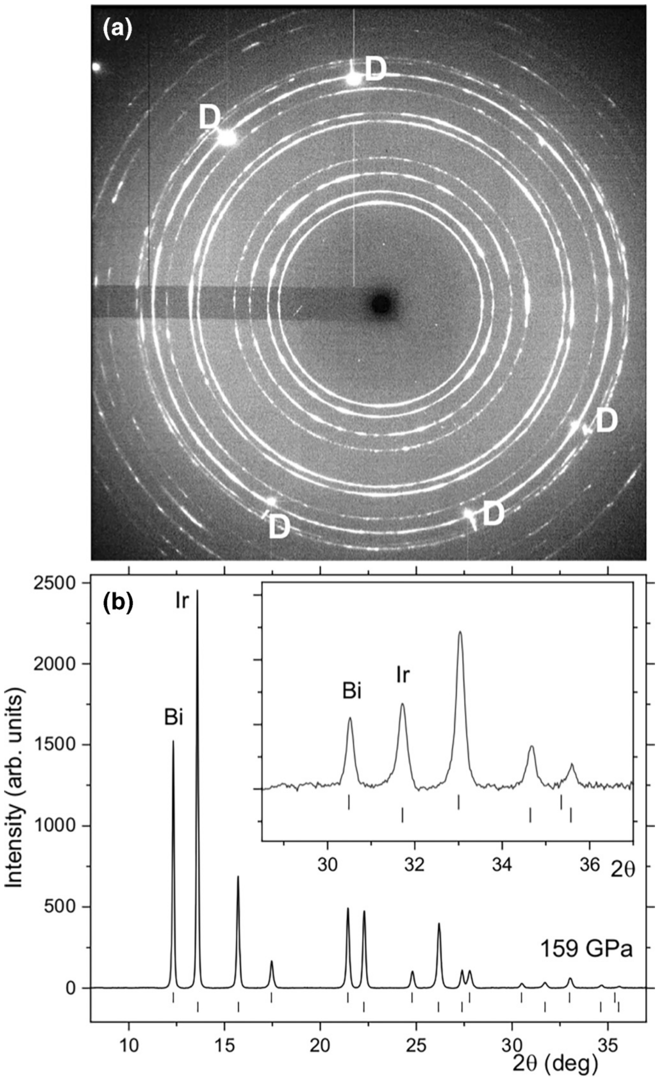

FIG. 2. (a) The 2D diffraction image obtained from Bi+Ir at 159 GPa, the highest pressure reached in this study, and (b) the background-subtracted 1D integrated profile at the same pressure. Diffraction features from the diamond anvils are labeled with D in (a). These and other nonsample diffraction features were masked prior to integrating the image to obtain the 1D profile. The narrow vertical lines in (a) are detector artifacts arising from the intense diamond reflections, and these were also masked prior to integration. The tick marks beneath the integrated profile in (b) show the calculated positions of the Bi (upper) and Ir (lower) diffraction peaks. The inset in (b) shows an enlarged view of the high-angle portion of the integrated profile. Eight or more diffraction peaks from the Ir were visible at all pressures, and this proved invaluable in determining the uniaxial stress component in the sample.

A. Sample stress environment

In the framework developed by Singh and coworkers [30–32], the uniaxial stress component t describes the difference between the axial stress σ_3 and the radial stress σ_1, i.e., $t = \sigma_3 - \sigma_1$. This can be quantified, since the lattice parameter obtained from different diffraction peaks $a_m(hkl)$, as measured in the standard transmission diffraction geometry, satisfies the following relationship:

$$a_m(hkl) = M_0 + M_1[3\Gamma(hkl)(1 - 3\sin^2\theta)]$$

where

$$\begin{aligned} M_0 &= a_P\{1 + (\alpha t/3)(1 - 3\sin^2\theta)[(S_{11} - S_{12}) \\ &\quad - (1 - \alpha^{-1})(2G_V)^{-1}]\}, \\ M_1 &= -a_P(\alpha S t/3), \\ \Gamma(hkl) &= (h^2k^2 + h^2l^2 + k^2l^2)/(h^2 + k^2 + l^2)^2, \\ S &= (S_{11} - S_{12} - S_{44}/2), \end{aligned}$$

where a_P is the lattice parameter in the absence of uniaxial stress, S_{ij} are the elastic compliances, θ is the diffraction angle, and G_V is the shear modulus of a randomly oriented polycrystalline aggregate under isostrain (Voigt) conditions. The parameter α weighs the contributions from the shear moduli under the conditions of stress continuity (Reuss) and strain continuity (Voigt) across the grain boundaries in the polycrystalline aggregate. $\alpha = 1$ corresponds to the condition of stress continuity, while $\alpha = 0.5$ corresponds to a condition halfway between the conditions of stress and strain continuity, and we have here assumed $\alpha = 1$.

Thus a plot of the measured $a_m(hkl)$ against $3\Gamma(hkl)(1 - 3\sin^2\theta)$ should be linear with slope M_1 and intercept M_0, and under the assumption that nonhydrostatic effects are relatively small, the uniaxial stress component t can be calculated from

$$t = -\frac{3}{\alpha S}\frac{M_1}{M_0}.$$

The maximum uniaxial stress component which can be supported by a material is equal to the material's yield strength σ_y, according to the von Mises yield criterion [33]. Put another way, a material with a high yield strength could, in principle, support a large uniaxial stress component. Maintaining a quasihydrostatic compression state in such a material therefore requires a PTM or other measures to maintain a low uniaxial stress component under pressure.

The yield strength of Ir increases from its ambient pressure value of 1 GPa to 5.5(11) GPa at a pressure of 165(9) GPa [34], providing a measure of the maximum uniaxial stress component a sample of Ir could support under strongly nonhydrostatic conditions. As shown in Fig. 3, compressing the Ir in a Bi PTM resulted in a maximum uniaxial stress component of only ∼1–2 GPa acting on the sample even above 150 GPa, attesting to the effectiveness of Bi as a PTM at pressures above 100 GPa. Indeed, our results imply that the Bi PTM maintained a hydrostatic environment comparable to that of a He PTM [35], and significantly better than that of a Ne PTM [36,37], making our measurements directly comparable with those of Monteseguro *et al.* [15], which were obtained to a maximum pressure of 137 GPa using a He PTM.

It has previously been noted that correcting the measured lattice parameters $a_m(hkl)$ for nonhydrostatic effects has the unfortunate side effect of increasing noise in the data [17,38]. For this reason, and motivated by the low uniaxial stress components observed in both the Bi calibrant and the Ir sample, we did not correct our measured lattice parameters in this study.

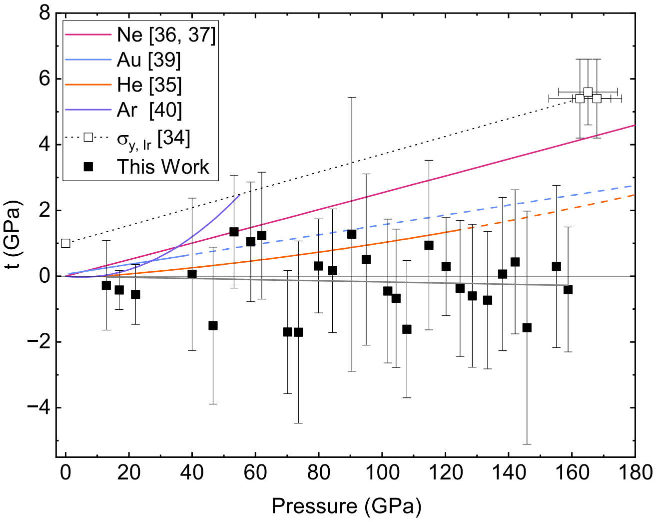

FIG. 3. The uniaxial stress component t measured in the Ir sample encased in a Bi PTM. Fits to previous measurements of the uniaxial stress components of Ne [36,37], Au [39], He [35], and Ar [40] are shown for comparison using different colored lines, and dashed portions of these lines are extrapolations of the measured values. The calculated yield strength $\sigma_{y,\mathrm{Ir}}$ for Ir are plotted using unfilled symbols and provide an upper bound for t [34], and the dotted line through these points is a guide to the eye. A linear fit (solid gray line) to the uniaxial stress data from Ir, with the intercept fixed at the origin, yields a slope of $-0.002(2)$. Uncertainties on t of Ir are propagated from uncertainties on M_1 and M_0.

B. Pressure and stress distribution

By collecting data from a 19 × 19 grid in 2-µm steps, we mapped out the pressure and stress environment in the sample chamber over a 36 µm × 36 µm area at periodic pressure increments. No diffraction from the W gasket was observed, indicating that the sample chamber was at least 40 µm in diameter. The pressure distribution observed at ∼150 GPa is shown in Fig. 4 and shows an approximately radially symmetric distribution, as expected. The corresponding distribution of the uniaxial stress component is shown in Fig. 5 with $t \approx 0$ GPa throughout. While the plot shows a lot of structure and inhomogeneity, these features fall within the approximately ±1-GPa uncertainty on the measurements at each point and are likely not physically meaningful. We recorded an average uniaxial stress component of $t = 0.2(6)$ GPa, where the uncertainty is the standard deviation.

The Ir grain, identified by a dashed outline in Figs. 4 and 5, has the effect of locally increasing the pressure on the Bi situated between the Ir and the anvil culets (Fig. 4), but we see no increase in the uniaxial stress component as a result (Fig. 5).

C. Compressive behavior and bulk modulus

The P-V compression data obtained in this investigation are shown in Fig. 6 together with those from previous investigations. We observe little scatter in our data, likely due to the use of a submicron x-ray beam FWHM and the strongly hydrostatic stress state of the sample resulting from the use of Bi as the PTM. See the Supplemental Material for data tables containing the volume measurements [41].

The compression data are plotted in linear $\eta_{\mathrm{APL}} - x$ space using Eq. (2) and are offset from each other for clarity (Fig. 7). We see that there is some unusual behavior in the low-pressure domain below 50 GPa but that the compressibility is linear above this pressure, i.e., $x \leqslant 0.96$. An arrow marks the

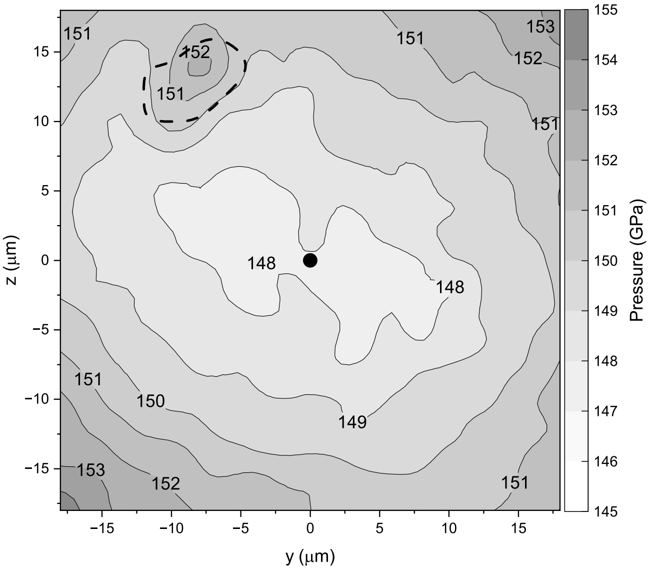

FIG. 4. The pressure distribution in the Bi-V PTM measured over the central 36 µm × 36 µm area of the sample. Diffraction data were collected every 2 µm in a 19 × 19 grid. The dashed outline marks the location of the Ir grain, and the black dot at the origin shows the 0.85 µm × 0.85 µm beam FWHM.

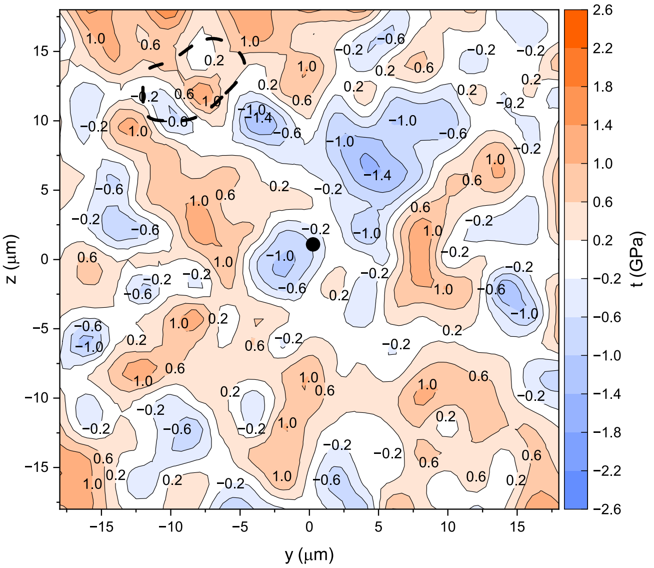

FIG. 5. Uniaxial stress components measured in the Bi-V PTM in 2-µm increments across a 36 µm × 36 µm area in a 19 × 19 grid. The typical uncertainty on each value is ∼1 GPa. The dashed outline marks the location of the Ir grain, and the black dot at the origin shows the 0.85 µm × 0.85 µm beam FWHM. Pressures are those shown in Fig. 4.

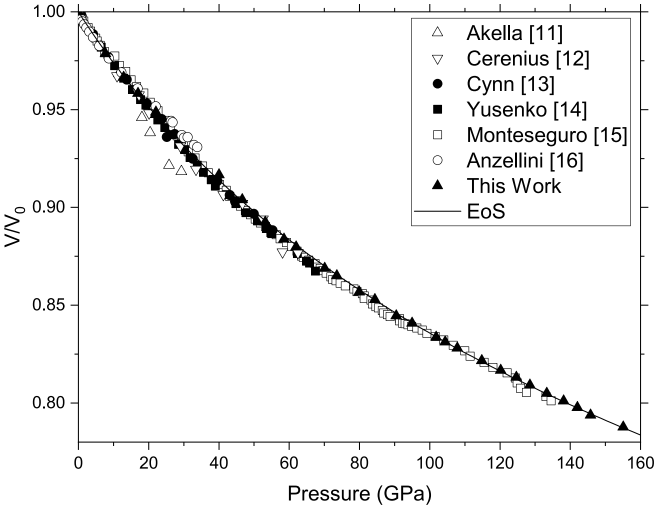

FIG. 6. The compression data of Ir from this work and the best-fitting BM EoS, with data from previous investigations [11–16].

location of the calculated CLC at 80 GPa, and it is clear that we see no anomaly at this pressure to indicate that any transition is occurring.

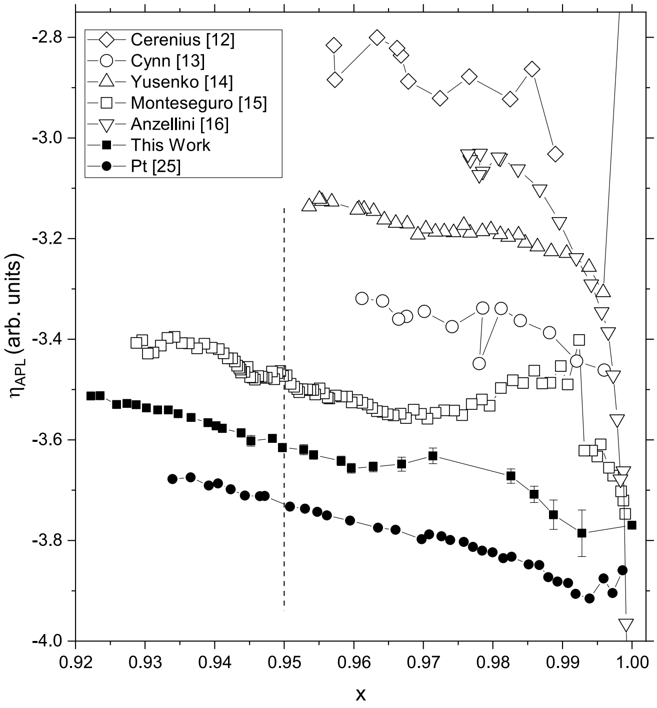

FIG. 7. The linearized compression data of Ir from this work (solid squares) with Pt (solid circles) for comparison from Dewaele *et al.* [25]. Linearized data from Refs. [12–16] (open symbols) are plotted with a 0.2 offset from each other in η_{APL} to improve clarity and facilitate comparison between the data. This offset results in the lowest pressure points from the data of Yusenko and Anzellini to lie above and below the graph, respectively. The dashed vertical line identifies the location CLC reported by Tal *et al.* at 80 GPa [9].

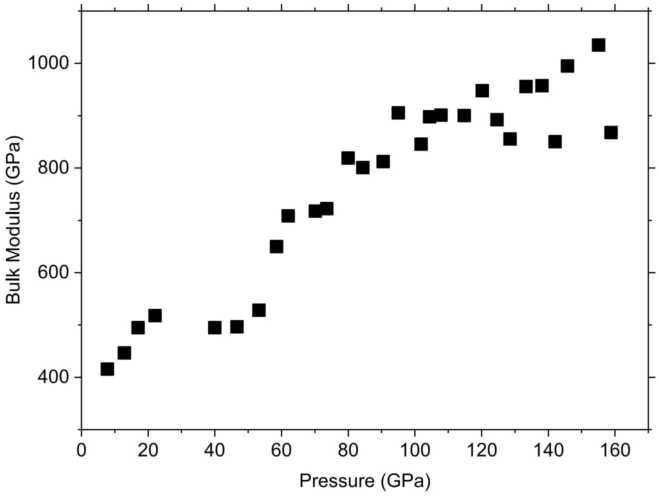

FIG. 8. The pressure dependence of the bulk modulus of Ir, calculated from adjacent data points upon compression.

The pressure dependence of the bulk modulus of Ir, $K(P)$, was calculated from

$$K(P) = -V\left(\frac{\Delta P}{\Delta V}\right),$$

where ΔP and ΔV are the difference between adjacent data points, and V is the average volume of these data. The resulting behavior of $K(P)$ is shown in Fig. 8. While there is some scatter in the data, and this crudely calculated bulk modulus is essentially constant between 30 and 60 GPa, there is no indication of an anomaly at 80 GPa which might indicate the presence of a CLC transition.

D. Equation of state

Vinet, Birch-Murnaghan (BM), AP1, and AP2 EoSs were fitted to our Ir compression data, and the best-fitting parameters in each case are shown in Table II. As said, we fixed the value of V_0 in all the fits at our measured value of 56.614(13) Å^3, which is larger than the value reported by Monteseguro *et al.* and Anzellini *et al.* [15,16] but is almost exactly equal to the weighted average of the published measurements shown in Table I [12–14,16], $\langle V_0 \rangle = 56.61(5)$ Å^3, where we have excluded the value published by Anzellini *et al.* [16] because it was reproduced from Monteseguro *et al.* [15].

We find that our BM values of $K_0 = 354(3)$ GPa and $K_0' = 5.03(9)$ are close to those measured in the most recent studies of Yusenko *et al.*, Monteseguro *et al.*, and Anzellini *et al.*, see Table I. The precision of our parameters is also very high, very similar to those obtained by Monteseguro *et al.* using a He PTM, likely owing to the submicron diameter x-ray beam used in our study, which would have mitigated pressure gradients within the probed sample volume, and the use of the Bi PTM. While a BM EoS resulted in the best fit to our data, resulting in the lowest weighted χ^2 value of 0.82, the Vinet and AP2 EoS produced comparable fits. The AP1 fit was somewhat worse due to this form only using one variable parameter, K_0.

TABLE II. The parameters, covariance $\sigma_{K_0K_0'}$, and weighted χ^2 for the best-fitting Vinet, Birch-Murnaghan (BM), AP1, and AP2 EoSs fitted to static high-pressure compression data obtained in this work, as well as best-fitting parameters for calculated compression data.

	Experiment				DFT	
	Vinet	BM	AP1	AP2	Vinet	BM
V_0 (Å^3/cell)	56.614(13)	56.614(13)	56.614(13)	56.614(13)	56.00	55.84
K_0 (GPa)	351(3)	354(3)	344.6(8)	353(3)	385	421
K_0'	5.29(9)	5.03(9)	–	5.15(10)	5.25	4.52
$\sigma_{K_0K_0'}$	–0.2693	–0.2739	–	–0.2962		
w-χ^2	0.9	0.82	1.09	0.85		

E. Summary

Our x-ray diffraction data to 159 GPa, and analysis of the compression curve, shows no evidence of any anomalies that would indicate the presence of a CLC transition at 80 GPa. However, our linearized data (Fig. 7) do exhibit an anomaly at lower pressures (∼30 GPa), which is also seen in the linearizations of the previous data of Monteseguro [15] and Anzellini [16] (see Fig. 1). This might suggest that there is indeed a CLC transition in Ir but that the calculated transition pressure was overestimated by Tal *et al.* [9]. In order to check this, we have therefore made our own electronic structure calculations of Ir for comparison with those of Tal *et al.*

V. COMPUTATIONAL STUDY

A. Computational methods

We calculated the total energy per unit cell of fcc Ir for a dense array of volumes ranging from 15.6 to 7.07 Å^3/atom, in steps of 0.14 Å^3, and covering pressures up to 1350 GPa. Calculations were conducted using the all-electron augmented-plane-wave with local-orbitals, (L)APW+lo, method as implemented by the WIEN2K code (Wien2k 21.1) [42]. Exchange-and-correlation effects were approximated using the meta-generalized gradient approximation by Sun *et al.* (SCAN) [43], and spin-orbit coupling was included. The radius of the muffin tins R_{MT} was set to 2.0 bohr^{-1}. This value is smaller than the default in order to prevent the muffin tins overlapping at small volumes. The choice of the muffin-tin radius does affect core-level energies; however, the effect is small compared to that from changing volume. The $5s$, $5p$, $4f$, $5d$, and $6s$ orbitals were treated as valence states, which allows them to extend outside the muffin tins.

A regular Monkhorst-Pack 40 × 40 × 40 grid of k points was used for sample the Brillouin zone. The largest Kohn-Sham plane-wave vector, $K_{\max}$, was given by $R_{\mathrm{MT}} \times K_{\max} = 11.0$. In order to ensure proper spin-orbit splitting of the $4f$ and $5p$ semicore states, the highest energy above the Fermi energy involved in the computation, $E_{\max}$, was increased to 30 Ry. The magnitude of the largest vector used in the charge-density Fourier expansion was set to $G_{\max} = 20\,\mathrm{bohr}^{-1}$. These parameters were greater than convergence tests indicated were necessary, in order to ensure small perturbations could be accurately calculated and numerical noise due to finite basis size was minimized.

There are several important differences between our methodology and that of Tal *et al.* [9]. Likely the most important is that we approximate the effect of exchange and correlation between the electrons using the SCAN

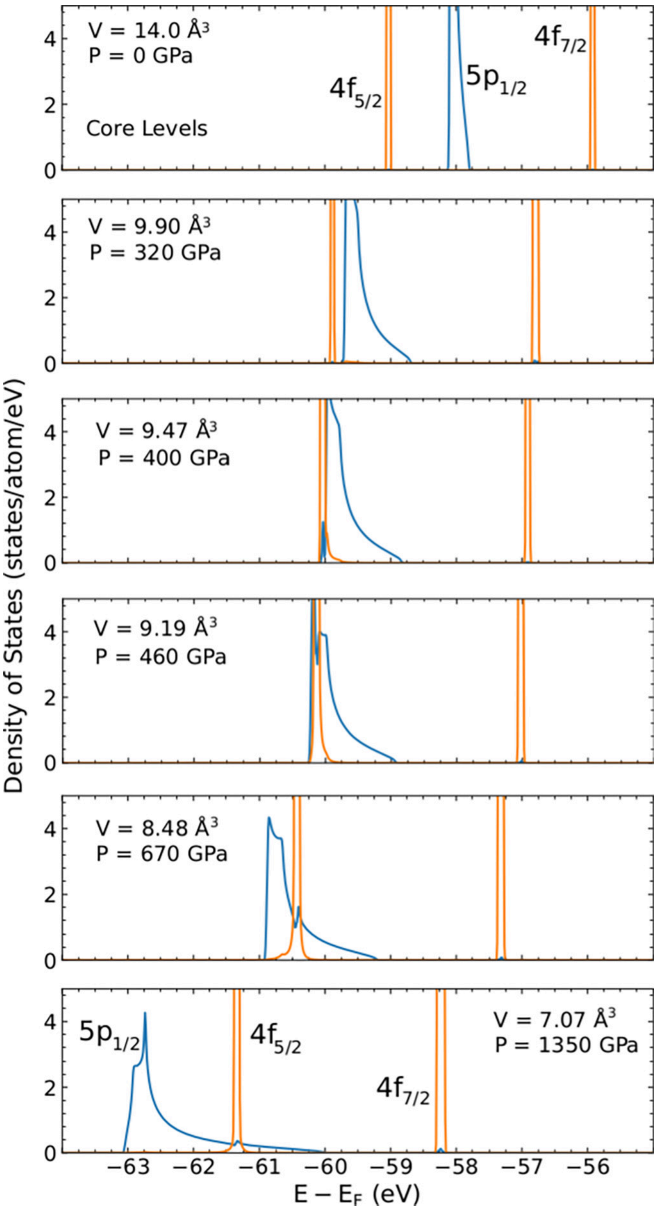

FIG. 9. Calculated projected density of states of the Ir core-level states at a range of pressures.

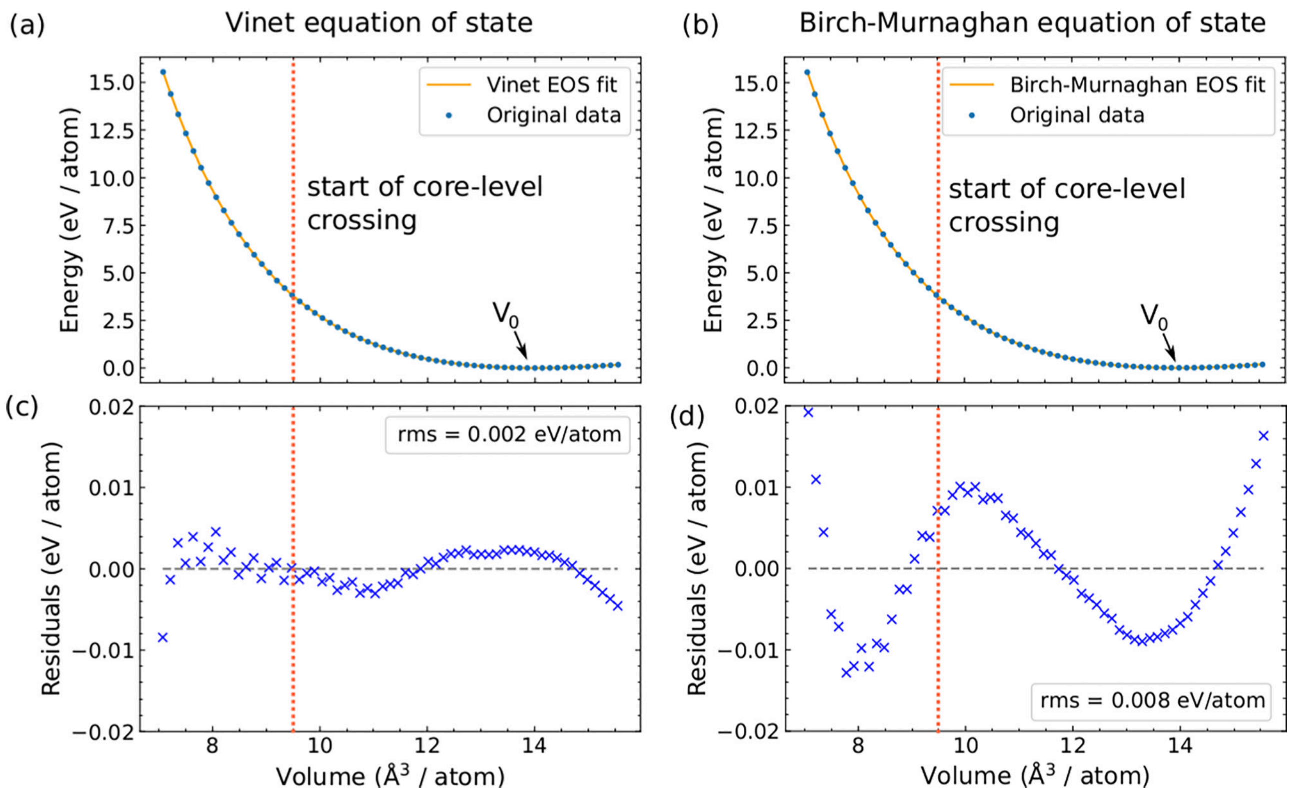

FIG. 10. Fits for the (a) Vinet and (b) third-order Birch-Murnaghan EoSs to the energy-volume data obtained from the DFT calculations. Panels (c) and (d) show the residuals from the fits on the same *y* scale. Note the root-mean-square of the residuals is 10^4 times smaller than the energy scale over which the EoSs are fitted. Fitting parameters can be found in Table II.

functional [43]. This functional obeys all known constraints on the exact exchange-correlation potential that a meta-GGA functional can. SCAN is known to achieve remarkable accuracy, especially for lattice constants and weak interactions. In contrast, Tal *et al.* used the local-density approximation (LDA), which is perhaps the simplest approximation for exchange-and-correlation interactions. LDA uses the exchange-and-correlation effects of a homogeneous free-electron gas and thus performs better for electronic structures similar to a free-electron gas such as simple metals. LDA is known to struggle with highly localized electronic states, such as *d* and *f* electrons. Further discussion can be found in the Supplemental Material [41].

B. Computational core-level crossing

Figure 9 shows the projected density of states of the core levels at different volumes. As volume decreases, the Fermi energy (E_F) increases—effectively moving the position of all core-level peaks lower in energy relative to E_F. At ambient conditions, the $4f_{5/2}$ shell is lower in energy than the $5p_{1/2}$ states. However, as the volume decreases, the energy of the $5p_{1/2}$ states drop relative to the $4f_{5/2}$ states, eventually crossing at volumes below approximately 9.5Å^3, corresponding to a pressure of 400 GPa, much greater than the 80 GPa predicted by Tal *et al.* [9]. The projected density of states shows some evidence of hybridization between the core levels: the lowest four plots in Fig. 9 show peaks in the *p*-type density of states located at the energy of the $4f_{5/2}$ peak. Furthermore, the $4f_{5/2}$ peak becomes more dispersed in energy after the crossing begins.

C. DFT equation of states

The calculations produce a fine grid of energy-pressure-volume data. We see in Fig. 10 that these data are very smooth, with no evidence of an anomaly at the CLC or elsewhere. The energy-volume data can be fitted well with either a Vinet (Fig. 10(a)) or Birch-Murnaghan (Fig. 10(b)) EoS. The Vinet EoS is based on the DFT calculations of Rose *et al.* [44] on a range of different materials, and so one would expect a good fit, as demonstrated by the residuals plot in Fig. 10(c). The resulting values of V_0, K_0, and K_0' are listed in Table II. The fit to the same data of the third-order Birch-Murnaghan EoS, which is based on linear elasticity theory and which does not accurately represent the volume variation of most solids under very high compression ($V/V_0 < 0.6$) [45], is somewhat poorer (Fig. 10(d)), and the values for K_0, K_0', and V_0 are rather different (Table II). Tempting as it might be to associate the peak in the BM EoS residual (Fig. 10(d)) with the CLC, the shape of the residual curve arises more straightforwardly from the inability of the BM EoS to fit the compression curve of Ir over such an extended range of V/V_0 (1.1 to 0.5). The shape of the residuals in Fig. 10(d) is that of a quartic. Thus, unsurprisingly, if a fourth-order Birch-Murnaghan EoS is used the peaks vanish and the fit is much improved.

D. DFT summary

Our DFT calculations show that the $4f_{5/2}$ and $5p_{1/2}$ levels cross above ∼400 GPa. This pressure is much higher than the 80 GPa predicted by Tal *et al.* [9], due to several differences in methodology. Furthermore, our calculations indicate that the CLC negligibly affects the compressibility of Ir.

Dubrovinsky *et al.* conducted DFT calculations on Os and saw no coupling between CLCs and the lattice parameters, in agreement with the calculations by Woolman and Ackland [10]. To explain this, Dubrovinsky *et al.* suggested that CLCs may only couple to thermal expansion coefficients, and thus the effect is only visible at finite temperatures. Computing thermal expansion properly requires the computation of anharmonic phonons, a complex and computationally intensive task, especially if core electrons must be included. However, the anomaly in the c/a ratio of Os observed by Dubrovinsky *et al.* is an order of magnitude greater than the change in c/a ratio due to thermal expansion from zero kelvin to room temperature at ambient pressure [46,47]. Even if the core-level crossing could completely negate thermal expansion along one axis of hcp Os, it still would not be enough to explain the anomaly seen in experiment. An alternative explanation, which is of the right order of magnitude, is elastic yield of the Os sample in the DAC [10].

VI. CONCLUSION

Motivated by previous DFT calculations reporting a core-level crossing (CLC) in Ir at 80 GPa, we have investigated Ir metal under hydrostatic conditions up to 160 GPa to search for the anomalous compression behavior that has been suggested to accompany such a transition. Having found no such anomaly, we have repeated the previous DFT calculations and find that the CLC occurs at the much higher pressure of 400 GPa.

Although pressures of this magnitude are experimentally attainable using double-stage or toroidal DACs, and while large changes in volume do affect the relative energies of core-level electron shells, our calculations show that the CLC has negligible effect on the compressibility. Indeed, our detailed calculations of the reported CLC in Os [10] led us to question whether core-level overlap has *any* measurable impact on the crystal structure in any material. Unfortunately, we know of no way of measuring the energies of the core levels at high pressures. While Auger and x-ray photoemission spectroscopies can accurately probe the fine structure of the core electrons, and indeed have been applied to the study of Ir and its oxides at ambient conditions [48,49], such techniques cannot be used on samples contained in DACs due to the complete absorption of the incident and emitted x rays/electrons within the ∼2-mm-thick diamond anvils used to compress the sample. Future theoretical work may reveal a link between core-level overlap and the crystal structure, or some other thermodynamic property, permitting experimental confirmation of such a transition. At present, the authors know of no convincing evidence for such a link.

This work also shows that using Bi as a solid-state PTM ensures the Ir sample is under hydrostatic stress to approximately 0.1% the Young's modulus of Ir. This is the kind of conditions needed to ensure anomalies, such as those seen by Dubrovinsky *et al.*, are not due to yielding events in the cell.

ACKNOWLEDGMENTS

British Crown Owned Copyright 2023/AWE. Published with permission of the Controller of His Britannic Majesty's Stationery Office. This work was supported by Grants No. EP/R02927X/1 and No. EP/S022155/1 from the UK Engineering and Physical Sciences Research Council (EPSRC). We acknowledge DESY (Hamburg, Germany), a member of the Helmholtz Association HGF, for the provision of experimental facilities. Parts of this research were carried out at Petra-III, and we would like to thank H.-P. Liermann, N. Giordano, and K. Glazyrin for their assistance in using beamline P02.2. Beam time was allocated for Proposal No. I-20211547. The authors would like to acknowledge the support of European Research Council (ERC) Grant "Hecate," Reference No. 695527, and the Engineering and Physical Sciences Research Council for UKCP Grant No. P022561. J.D.M. is grateful to AWE for the award of CASE Studentship P030463429.

---

[1] H. Tups, K. Takemura, and K. Syassen, Phys. Rev. Lett. **49**, 1776 (1982).

[2] K. Takemura and K. Syassen, Solid State Commun. **44**, 1161 (1982).

[3] G. K. Samudrala and Y. K. Vohra, in *Handbook on the Physics and Chemistry of Rare Earths: Including Actinides*, edited by J.-C. G. Bünzli and V. K. Pecharsky (Elsevier, New York, 2013), Vol. 43, pp. 275–319.

[4] K. A. Goettel, J. H. Eggert, I. F. Silvera, and W. C. Moss, Phys. Rev. Lett. **62**, 665 (1989).

[5] H. Luo, S. Desgreniers, Y. K. Vohra, and A. L. Ruoff, Phys. Rev. Lett. **67**, 2998 (1991).

[6] T. Kenichi, Phys. Rev. Lett. **75**, 1807 (1995).

[7] T. L. Underwood, G. J. Ackland, and R. J. Cole, Phys. Rev. B **90**, 014201 (2014).

[8] L. Dubrovinsky, N. Dubrovinskaia, E. Bykova, M. Bykov, V. Prakapenka, C. Prescher, K. Glazyrin, H.-P. Liermann, M. Hanfland, M. Ekholm, Q. Feng, L. V. Pourovskii, M. I. Katsnelson, J. M. Wills, and I. A. Abrikosov, Nature (London) **525**, 226 (2015).

[9] A. A. Tal, M. I. Katsnelson, M. Ekholm, H. J. M. Jönsson, L. Dubrovinsky, N. Dubrovinskaia, and I. A. Abrikosov, Phys. Rev. B **93**, 205150 (2016).

[10] G. A. Woolman and G. J. Ackland, Phys. Rev. B **106**, L081102 (2022).

[11] J. Akella, J. Phys. Chem. Solids **43**, 941 (1982).

[12] Y. Cerenius and L. Dubrovinsky, J. Alloys Compd. **306**, 26 (2000).

[13] H. Cynn, J. E. Klepeis, C.-S. Yoo, and D. A. Young, Phys. Rev. Lett. **88**, 135701 (2002).

[14] K. V. Yusenko, S. Khandarkhaeva, T. Fedotenko, A. Pakhomova, S. A. Gromilov, L. Dubrovinsky, and N. Dubrovinskaia, J. Alloys Compd. **788**, 212 (2019).

[15] V. Monteseguro, J. A. Sans, V. Cuartero, F. Cova, I. A. Abrikosov, W. Olovsson, C. Popescu, S. Pascarelli, G. Garbarino, H. J. M. Jönsson, T. Irifune, and D. Errandonea, Sci. Rep. **9**, 8940 (2019).

[16] S. Anzellini, L. Burakovsky, R. Turnbull, E. Bandiello, and D. Errandonea, Crystals **11**, 452 (2021).

[17] C. V. Storm, J. D. McHardy, M. J. Duff, S. G. MacLeod, E. F. O'Bannon, and M. I. McMahon, J. Appl. Phys. **133**, 245904 (2023).

[18] E. J. Pace, S. E. Finnegan, C. V. Storm, M. Stevenson, M. I. McMahon, S. G. MacLeod, E. Plekhanov, N. Bonini, and C. Weber, Phys. Rev. B **102**, 094104 (2020).

[19] S. E. Finnegan, E. J. Pace, C. V. Storm, M. I. McMahon, S. G. MacLeod, H.-P. Liermann, and K. Glazyrin, Phys. Rev. B **101**, 174109 (2020).

[20] S. E. Finnegan, C. V. Storm, E. J. Pace, M. I. McMahon, S. G. MacLeod, E. Plekhanov, N. Bonini, and C. Weber, Phys. Rev. B **103**, 134117 (2021).

[21] S. E. Finnegan, M. G. Stevenson, E. J. Pace, C. V. Storm, J. D. McHardy, M. I. McMahon, S. G. MacLeod, E. Plekhanov, N. Bonini, and C. Weber, Phys. Rev. B **105**, 174104 (2022).

[22] C. V. Storm, J. D. McHardy, S. E. Finnegan, E. J. Pace, M. G. Stevenson, M. J. Duff, S. G. MacLeod, and M. I. McMahon, Phys. Rev. B **103**, 224103 (2021).

[23] W. B. Holzapfel, Rep. Prog. Phys. **59**, 29 (1996).

[24] W. B. Holzapfel, High Press. Res. **16**, 81 (1998).

[25] A. Dewaele, P. Loubeyre, and M. Mezouar, Phys. Rev. B **70**, 094112 (2004).

[26] H.-P. Liermann, Z. Konôpková, W. Morgenroth, K. Glazyrin, J. Bednarčik, E. E. McBride, S. Petitgirard, J. T. Delitz, M. Wendt, Y. Bican, A. Ehnes, I. Schwark, A. Rothkirch, M. Tischer, J. Heuer, H. Schulte-Schrepping, T. Kracht, and H. Franz, J. Synchrotron Radiat. **22**, 908 (2015).

[27] K. Glazyrin, S. Khandarkhaeva, T. Fedotenko, W. Dong, D. Laniel, F. Seiboth, A. Schropp, J. Garrevoet, D. Brückner, G. Falkenberg, A. Kubec, C. David, M. Wendt, S. Wenz, L. Dubrovinsky, N. Dubrovinskaia, and H.-P. Liermann, J. Synchrotron Radiat. **29**, 654 (2022).

[28] C. Prescher and V. B. Prakapenka, High Pressure Res. **35**, 223 (2015).

[29] T. J. B. Holland and S. A. T. Redfern, Mineral. Mag. **61**, 65 (1997).

[30] A. K. Singh, J. Appl. Phys. **73**, 4278 (1993).

[31] A. K. Singh and C. Balasingh, Bull. Mater. Sci. **19**, 601 (1996).

[32] A. K. Singh, C. Balasingh, H.-K. Mao, R. J. Hemley, and J. Shu, J. Appl. Phys. **83**, 7567 (1998).

[33] A. L. Ruoff, J. Appl. Phys. **46**, 1389 (1975).

[34] J. L. Brown, J.-P. Davis, and C. T. Seagle, J. Dyn. Behav. Mater. **7**, 196 (2021).

[35] K. Takemura, High Pressure Res. **41**, 155 (2021).

[36] Y. Meng, D. J. Weidner, and Y. Fei, Geophys. Res. Lett. **20**, 1147 (1993).

[37] K. Takemura, T. Watanuki, K. Ohwada, A. Machida, A. Ohmura, and K. Aoki, J. Phys.: Conf. Ser. **215**, 012017 (2010).

[38] K. Takemura and A. Dewaele, Phys. Rev. B **78**, 104119 (2008).

[39] T. S. Duffy, G. Shen, D. L. Heinz, J. Shu, Y. Ma, H.-K. Mao, R. J. Hemley, and A. K. Singh, Phys. Rev. B **60**, 15063 (1999).

[40] H.-K. Mao, J. Badro, J. Shu, R. J. Hemley, and A. K. Singh, J. Phys.: Condens. Matter **18**, S963 (2006).

[41] See Supplemental Material at http://link.aps.org/supplemental/10.1103/PhysRevB.109.024101 for tables of PV data, details on corrections for nonhydrostatic effects, and further details on the DFT calculations presented in this work, which includes Refs. [9,10,15,17,43,44].

[42] P. Blaha, K. Schwarz, F. Tran, R. Laskowski, G. K. Madsen, and L. D. Marks, J. Chem. Phys. **152**, 074101 (2020).

[43] J. Sun, R. C. Remsing, Y. Zhang, Z. Sun, A. Ruzsinszky, H. Peng, Z. Yang, A. Paul, U. Waghmare, X. Wu, M. L. Klein, and J. P. Perdew, Nat. Chem. **8**, 831 (2016).

[44] J. H. Rose, J. R. Smith, and J. Ferrante, Phys. Rev. B **28**, 1835 (1983).

[45] R. J. Angel, M. Alvaro, and J. Gonzalez-Platas, Z. Kristallogr. - Cryst. Mater. **229**, 405 (2014).

[46] J. W. Armblaster, Platinum Met. Rev. **57**, 177 (2013).

[47] Y. S. Touloukian, R. K. Kirby, R. E. Taylor, and P. D. Desai, *Thermophysical Properties of Matter* (Defense Technical Information Center, 1975), Vol. 12, p. 244.

[48] V. Pfeifer, T. E. Jones, J. J. V. Vélez, C. Massué, R. Arrigo, D. Teschner, F. Girgsdies, M. Scherzer, M. T. Greiner, J. Allan, M. Hashagen, G. Weinberg, S. Piccinin, M. Hävecker, A. Knop-Gericke, and R. Schlögl, Surf. Interface Anal. **48**, 261 (2016).

[49] S. J. Freakley, J. Ruiz-Esquius, and D. J. Morgan, Surf. Interface Anal. **49**, 794 (2017).